

Polyaniline–Polypyrrole Composites for Improved Energy Storage: A Critical Evaluation

Aranganathan Viswanathan,* Prakashaiah B. G., and Vanchiappan Aravindan*

The well-known two conducting polymers, polyaniline (PANI) and polypyrrole (PPy), are experimented for their synergy in improving their energy storage property in the form of symmetric supercapacitors using aqueous acidic electrolyte 1 M H₂SO₄. The results of the energy storage study reveal that there is no synergy established nor an increase in energy storage of PANI attained. Instead, a decrease in energy storage of PANI is attained when combined with PPy, which is due to the reduction in the aspect ratio, and faradaic surface area. These results are confirmed by the Brunauer–Emmett–Teller surface analysis and supported by the

density functional theory studies. However, the addition of a minimal amount of PPy to PANI increases the rate capability of PANI significantly, with a slight decrease in its energy storage. In addition, the addition of PANI to PPy increases the energy storage of PPy to a larger extent. Therefore, it would be a negative notion to combine PANI and PPy to increase their overall energy storage. The obtained specific capacity (*Q*), specific energy (*E*), specific power (*P*), and coulombic efficiency (η) of PANI are 74.82 C g⁻¹, 12.47 Wh kg⁻¹, 0.6 kW kg⁻¹, and 93.57 %, respectively.

1. Introduction

The carbonaceous materials like activated carbon, graphene, reduced graphene oxide, etc., and a plethora of metal oxides and hydroxides like CuO, NiO, Ni(OH)₂, CoO, Fe₂O₃, TiO₂, etc., have been explored for their energy storage and delivery processes, both individually and as composites, in order to produce efficient supercapacitor electrodes. However, the objective of achieving supercapacitors with high energy in the order of batteries and with high power has not yet been achieved due to the limitations associated with the carbonaceous and metal oxide/hydroxides. The limitations of carbonaceous materials are their low specific capacitance due to the surface-limited electrical double-layer formation mechanism (surface process); however, they exhibit good electrical conductivity, specific power (*P*), and durability. The limitations associated with metal oxides are their poor electrical conductivity, brittle nature, and low durability caused by it, lower rate capability, and poor *P*; however, they provide higher specific capacity (*Q*) due to faradaic energy storage mechanisms (redox reactions and intercalation processes (bulk processes)) and higher specific energy (*E*).^[1–3]

Amongst the different supercapacitor electrodes available, the conducting polymers (CPs) have intriguing and beneficial features that set them higher than the other materials. The structural and electrochemical properties of CPs can be engineered via different chemical combinations, structural designs, and fabrication techniques, and these techniques enhance their electrochemical active surface area, the kinetics of ionic diffusion, and electron transport, thus imparting superior performance in supercapacitors. The CP-containing supercapacitors have been extensively explored in different configurations to produce micro-, fiber-, flexible, and stretchable supercapacitors. Conducting polymers possess the delocalized *p*-electron system along their backbone, forming a conjugated backbone. These conjugated backbones are formed by the overlapping of their molecular orbitals. As the length of conjugation on the polymer backbone increases, a large number of molecular orbitals interact to form a series of discrete energy levels that can be occupied or unoccupied with electrons, which are called bonding π orbitals and anti-bonding π^* orbitals, respectively. These bonding and antibonding energy levels are separated by an energy bandgap. The energy levels on either side of the bandgap are called HOMO (highest occupied molecular orbital (π -bonding orbitals)) and LUMO (lowest unoccupied molecular orbital (π^* -antibonding orbitals)). The electric conduction of CPs occurs when free charge carriers are created during the doping process. During the doping process, electrons are either added to or removed from the molecular orbitals of the CPs. When electrons migrate from the HOMO to the LUMO, the CPs become conducting as the charge movement occurs through the hopping of electrons along the backbone of the polymer by the continuous overlapping of π orbitals. However, the CPs suffer the charge localization effects, which is caused by charge trapping when the CPs have highly disordered structures, where the connectivity between the polymer chains is absent. This phenomenon limits the electronic conductivity of the CPs. The CPs exhibit electrical conductivity by the movement of either

A. Viswanathan, V. Aravindan
Department of Chemistry
Indian Institute of Science Education and Research (IISER)
Tirupati, Andhra Pradesh 517619, India
E-mail: ranguchemist@gmail.com
aravindan@iisertirupati.ac.in

P. B. G.
Corrosion Area
Chemical and Material Sciences Division
CSIR-Indian Institute of Petroleum
Dehradun 248005, India

 Supporting information for this article is available on the WWW under <https://doi.org/10.1002/batt.202500334>

electrons or holes along the conjugated bonds in their chemical structure. They also exhibit mixed electronic and ionic conduction. Polypyrrole (PPy), polyaniline (PANI), polyindole,^[4–6] and polythiophene (theoretical capacitance 485 F g^{-1} ^[7]), and their derivatives like 3,4-ethylenedioxy thiophene (theoretical capacitance 210 F g^{-1} ^[8]) and polyparafluorophenylthiophene^[9] are a few extensively studied supercapacitor electrode materials. These CPs possess the following indispensable advantages: biocompatibility, chemical stability in different aqueous electrolytes and in organic solvents, tunable mechanical properties like flexibility, softness, and low Young's modulus, low temperature solution processability to attain thin films, 3D composites, fibers, etc., and various synthetic routes.^[10–12]

The CPs like PANI, PPy, etc., bridge carbonaceous and metal-based materials as they can provide both *P* and *E* by the faradaic reactions that occur on their backbone (doping and dedoping of a proton). However, the limitation associated with them is their poor cyclic stability due to the significant volume variations that they undergo during the charge storage/delivery processes.^[11] Therefore, when this volume variation is prevented or reduced, they can be a beneficial supercapacitor electrode. It is anticipated that when the CPs of the right kind, in the right proportion are combined, their properties will vary, but the fruitfulness of such combinations is uncertain. Therefore, this study explores the effect of composites of CPs in energy storage as supercapacitor electrodes.

Among the various CPs, PANI, and PPy have immense merits and commonalities. The merits and commonalities that both the CPs possess are facile synthesis using the same oxidizing agents and dopants, inexpensiveness, non-toxicity, high theoretical specific capacitance (PANI 2000 F g^{-1} ^[13] and PPy 3400 F g^{-1} ^[14]), high conductivity, storage of energy by reversible faradaic processes, fast doping and dedoping, environmental friendliness, etc.^[15–17] The limitation of both CPs is their poor durability due to the significant volumetric alterations that they undergo during the charging and discharging processes.^[18] Specifically, the low durability of PPy is due to the pulverization and counter-ion drain effect that it experiences during the charging/discharging process. During the course of oxidation of PPy, the nitrogen groups with positive charges are created on PPy chains; then, so as to neutralize the charge, counter-ions migrate onto the backbones from the electrolyte, causing the swelling of PPy. During the reduction, polarons are balanced by the injected electrons and the counter-ions migrate back into the electrolyte, causing shrinkage in PPy. This continuous process of swelling and shrinkage leads to the structural pulverization of PPy and in turn, a reduction in the energy storage. On the other hand, the counter-ion drain effect of PPy occurs when its backbone takes up only a few anions after cycling for doping due to the irreversible insertion/extrusion of counterions. Therefore, this irreversible counter-ion doping will decrease the electrical conductivity of PPy and in turn, lead to poor durability.^[19] It is reported that the use of sulfonate anions as a dopant and carbon materials, like partially exfoliated graphite (as it can alleviate the pulverization effect by accommodating the volumetric expansion) as a flexible substrate, could improve the durability of PPy against the continuous charging and discharging.^[19] It is also reported that the PPy

provides lower energy storage performance when used alone due to its low ion transfer in redox reaction due to its poor electrical conductivity, resulting in a lower-specific capacitance than its theoretical prediction.^[20] In addition, it is difficult to synthesize PPy with a regular structure and a large specific surface area.^[20]

A few reported performances of PANI and PPy composites are as follows: 1) PANI nanowires wrapped on the PPy nanotubes: 765 F g^{-1} at 10 mV s^{-1} (3-electrode (EL) system),^[20] 2) PPy–PANI co-axial nanoarray: 64.5 F g^{-1} at 0.5 A g^{-1} (2-EL system),^[21] 3) PANI–PPy nanocomposite: 737 F g^{-1} at a scan rate of 5 mV s^{-1} ,^[22] and 4) PPy–PANI nanospheres: 510 F g^{-1} at 10 mV s^{-1} (3-EL system).^[23] These performances of the composites are not up to the theoretical capacitances of neither PANI nor PPy. Therefore, further exploration of the composites of PANI and PPy (PP), and its concentration-dependent optimizations are essential and so is this study.

In this study, the PANI and PPy nanocomposites were synthesized at different weight compositions, and their structural features and energy storage performances are presented. The density functional theory (DFT) analyses that are conducted on PANI, PPy, and PANI + PPy are also presented as a support for the experimental data obtained.

2. Structural Characterizations

2.1. XRD and Fourier-transform infrared spectroscopy (FTIR) Analyses

The XRD patterns of PANI, PPy, and PANI + PPy (Figure 1) have broader peaks with the peak maxima at 24.33° , 19.90° , and 24.13° , respectively, covering the region of 2θ between 13° to 36° , 13° to 34° , and 14° to 35° , respectively. The peak of 24.33° of PANI corresponds to the (200) plane of PANI.^[24] The peak at 19.90° ^[25] and 24.27° ^[26] are of PPy. Again, the broad peak of PANI + PPy contains the peaks of both PANI and PPy. The low-intense, broad peaks of

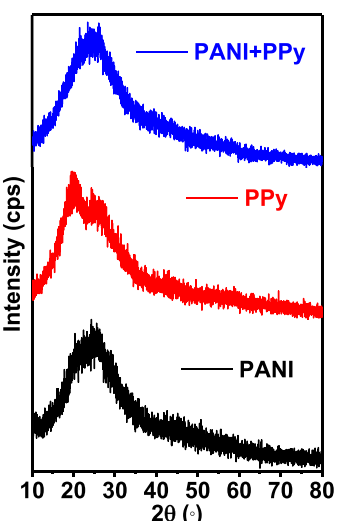


Figure 1. X-ray diffraction patterns of PANI, PPy, and PANI + PPy.

PANI, PPy, and PANI + PPy indicate their low crystalline nature. The crystallite size (Equation S1, Supporting Information) of PANI and PANI + PPy corresponding to the peak positions of 24.33° and 24.13° are 0.49 and 0.48 nm, respectively. Since the two peaks of PPy are only separated at the top of the peak, the full width at half maximum that is common to both peaks were used to calculate the crystallite size of PPy, and the crystallite size obtained was 0.52 nm, which was higher than both of PANI and PANI + PPy. It is to be remarked that the broadness of the peaks of PANI, PPy, and PANI + PPy are similar and therefore, rationalize the point of comparison of their crystallite sizes. The PANI, PPy, and PANI + PPy with such low intensity and broadness are already reported.^[24,27–30]

The transmittances present in the IR spectrum of PANI (Figure 2) (Table S1, Supporting Information) are at 694 (C=C stretching vibrations), 879 (C—H out-of-plane bending vibrations), 1042 (C=N stretching vibrations), 1144 (C—H in-plane bending vibrations), 1291 (C—N stretching vibrations), 1488 (C=C stretching vibrations of benzenoid rings), and 1566 cm^{-1} (C=C stretching vibrations of quinoid ring).^[24] The transmittances present in the IR spectrum of PPy (Figure 2) (Table S1, Supporting Information) are at 793 (C—H wagging),^[31] 914 (the C—H out-of-plane deformations of the ring),^[32] 964 (the doped state of PPy by sulfonic acid),^[33] 1045 (C—H and N—H in-plane deformations),^[32] 1097 (N—H⁺ deformations),^[32] 1192 (breathing modes of PPy),^[32,33] 1297 (characteristic of oxidized (doped) PPy or to the

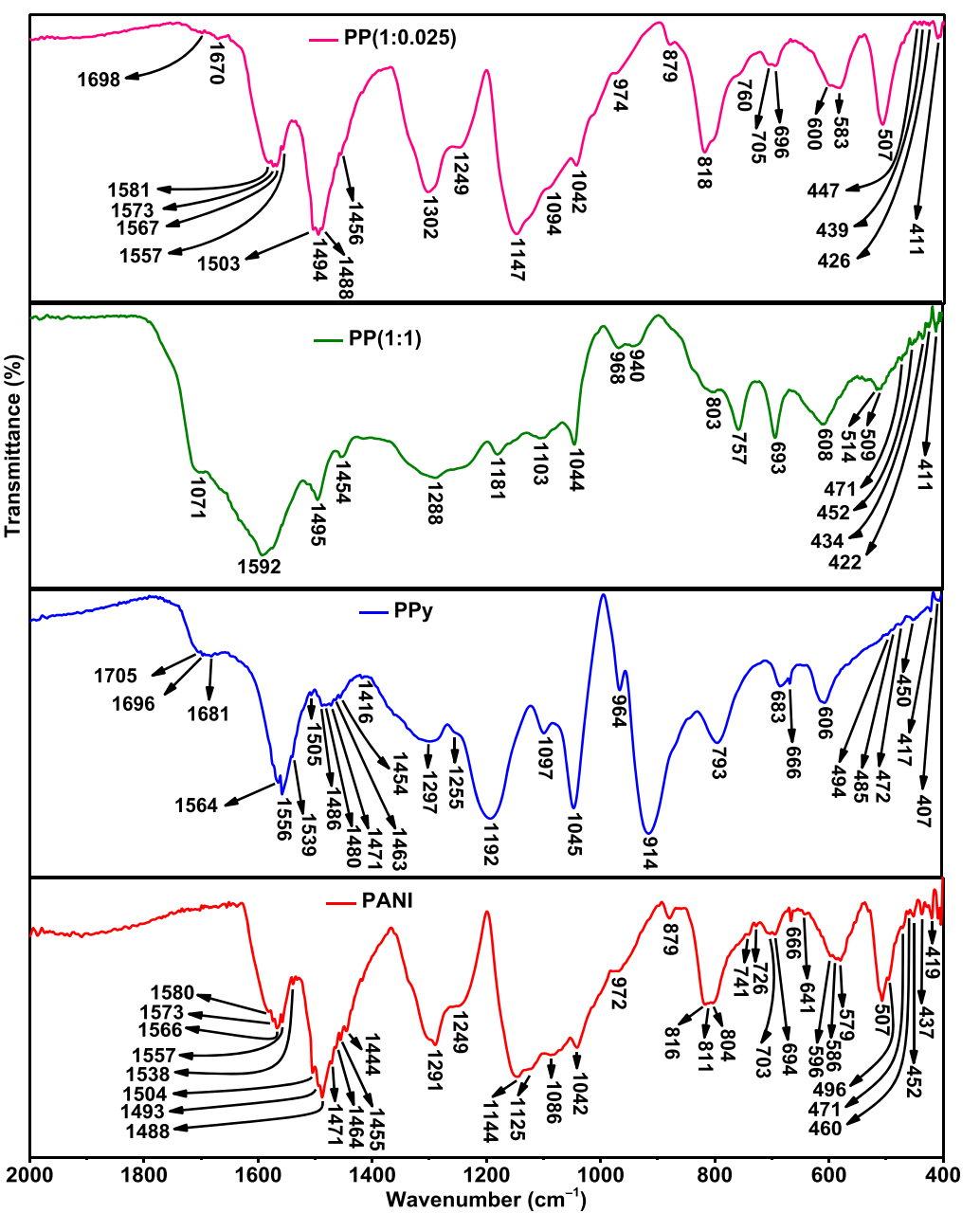


Figure 2. FTIR spectra of PANI, PPy, PP(1:1), and PP(1:0.025).

effective conjugation length),^[33] 1480 (C—N stretching vibrations of pyrrole ring),^[32] 1556 (C—C stretching vibrations in the pyrrole ring),^[32] and 1681 cm⁻¹ (fundamental vibration of pyrrole ring).^[34]

The transmittances present in the IR spectra of the composites of PPs (Figure 2, S2a, S2b, and S2c, Supporting Information) possess transmittances of both PANI and PPy. The IR peaks of PANI are predominantly seen in the IR spectra of PPs. The IR peak positions of PANI, PPy, and PPs are given in Table S1.

As per Ref.,[6] The IR bands of the copolymer of aniline and pyrrole shift to lower wavenumbers with respect to their homopolymers, while another study^[12] shows the contrary. Therefore, there is no authentic method to determine the formation of copolymers of aniline and pyrrole. In addition, the literature presenting the copolymers of aniline and pyrrole contains the characteristic IR bands of both PANI and PPy. Therefore, it is difficult to conclude the formation of a copolymer of aniline and pyrrole, but it is evident that the mixture of PANI and PPy is present, as indicated by the IR spectrum of PPs. However, some insignificant changes in IR bands of PPs were observed with respect to those of PANI and PPy, which indicates that there is some interaction between the PANI and PPy present. In addition, it is to be noted from Table S1, Supporting Information, that the main IR band of PANI and PPy, like C=C stretching, C—N stretching, and C=N stretching, are either unaltered or slightly shifted to higher wavenumbers. Therefore, it is perceived that the PPs are made up of a composite of PANI and PPy, not the copolymer of PANI and PPy. This deduction is further supported by the video S1.

As shown in video S1, upon adding the reagents at the same time into the reaction chambers of both aniline and pyrrole, the initiation of polymerization of pyrrole takes place immediately, while that of aniline takes place after 5 min. Moreover, in these 5 min, a thick slurry of PPy is formed. Because of this time difference, the chances of the formation of a copolymer of aniline and pyrrole are unlikely, but their homopolymer forms.

The main peaks of PP(1:0.025) (Figure 2) are at 696 (C—C stretching vibrations),^[24] 760 (C—H out-of-plane bending), 974 (the doped state of PPy by sulfonic acid),^[33] 1042 (C=N stretching vibrations in PANI and N—H in-plane stretching vibrations in PPy^[35]), 1146 (C—H in-plane bending vibrations), 1302 (C—N stretching in PANI^[24] and C—C stretching in PPy^[35]), 1456 (C—N stretching in PPy),^[32] 1494 (C=C stretching vibrations of benzeneoid rings of PANI and corresponding to PPy rings^[27,36]), and 1581 cm⁻¹ (corresponding to C=C stretching vibrations of quinoid ring).^[36] All the transmittances of PANI, PPy, and PANI + PPy confirm their successful synthesis.

2.2. X-ray photoelectron spectroscopy (XPS) Analyses

The XPS studies of PANI are detailed in our earlier study.^[24] The XPS survey spectrum of PPy (Figure 3a) and PANI + PPy (Figure 3b) contain all the elements of PPy and PANI. The deconvolutions of the core-level spectrum of C 1s, N 1s of PPy (Figure 3c,d) and PANI + PPy (Figure 3e,f) confirm the presence of species of PPy and PANI (Table 1). The deconvolutions of the core level spectrum of O 1s, S 2p of PPy (Figure S3a and

Figure S3b, Supporting Information) and of PANI + PPy (Figure S3c and S3d, Supporting Information) are provided in the supporting information.

2.3. FESEM Analyses

The FESEM images of PPy (Figure 4a,b), PANI (Figure 4c,d), and PANI + PPy (Figure 4e,f) depict that they possess particle (0D), fiber (1D), and particle (0D) morphology, respectively. The particle diameters of PPy and PANI + PPy range from 270 to 470 nm (Figure S4, Supporting Information) and 100 to 220 nm (Figure S5, Supporting Information), respectively. The fiber diameter of PANI is in the range of 34 to 52 nm (Figure S6, Supporting Information). The FE-SEM images of PPy, PANI, and PANI + PPy also depict the presence of channels on their structures that allow the permeation of electrolytes into them during the energy storage and delivery processes. These magnitude of channels are in the order of PANI > PANI + PPy > PPy, and the diameters of these channels are micro and meso in the cases of PPy, PANI + PPy, and PANI, respectively. The mesochannels of PANI enable the effective diffusion of electrolytes in PANI in relation to PPy and PANI + PPy. This effective diffusion of electrolyte in PANI reduces its intrinsic resistance, increases its conductivity, and in turn, enables it to store a higher magnitude of energy. Meanwhile, among PPy and PANI + PPy, the latter has a moderate number of channels for electrolytic diffusion and thus, exhibits lower resistance, higher conductivity, and relatively higher energy storage than the former. The lower fiber diameter and nanostructure of PANI enable it to exhibit a higher faradaic active surface area for the process of energy storage and delivery compared with PPy and PANI + PPy. The bigger particle sizes of PPy and PANI + PPy are due to the faster polymerization of pyrrole, and this faster polymerization of pyrrole leads to undersaturated and heterogeneous nucleation centers, which causes the aggregation of PPy (Video S1). In addition, the self-adhesion character of PPy also contributes to its agglomeration.^[19] The faradaic surface area offered is in the order of PANI > PANI + PPy > PPy, and this is further confirmed by Brunauer–Emmett–Teller (BET) surface analyses.

2.4. BET Surface Analyses

The BET adsorption isotherms of PANI, PPy, and PP(1:0.025) (Figure 5a) depict that the volume of N₂ adsorption is in the order of PANI > PP(1:0.025) > PPy. This order confirms that the maximum surface area offered is by PANI, and the order of surface area follows the order of volume of N₂ adsorption. The BET surface area of PANI, PPy, and PP(1:0.025) are 36.93, 20.17, and 27.05 m² g⁻¹, respectively. Figure 5b,c indicate that the PANI, PPy, and PP(1:0.025) majorly possess the mesopores. The pore volumes and the corresponding surface area offered are higher in the case of PANI. These observations indicate that the addition of PPy to PANI negatively affects the character of PANI. At the same time, it is important to be noted that the addition of PANI to PPy increases the properties of PPy favorably.

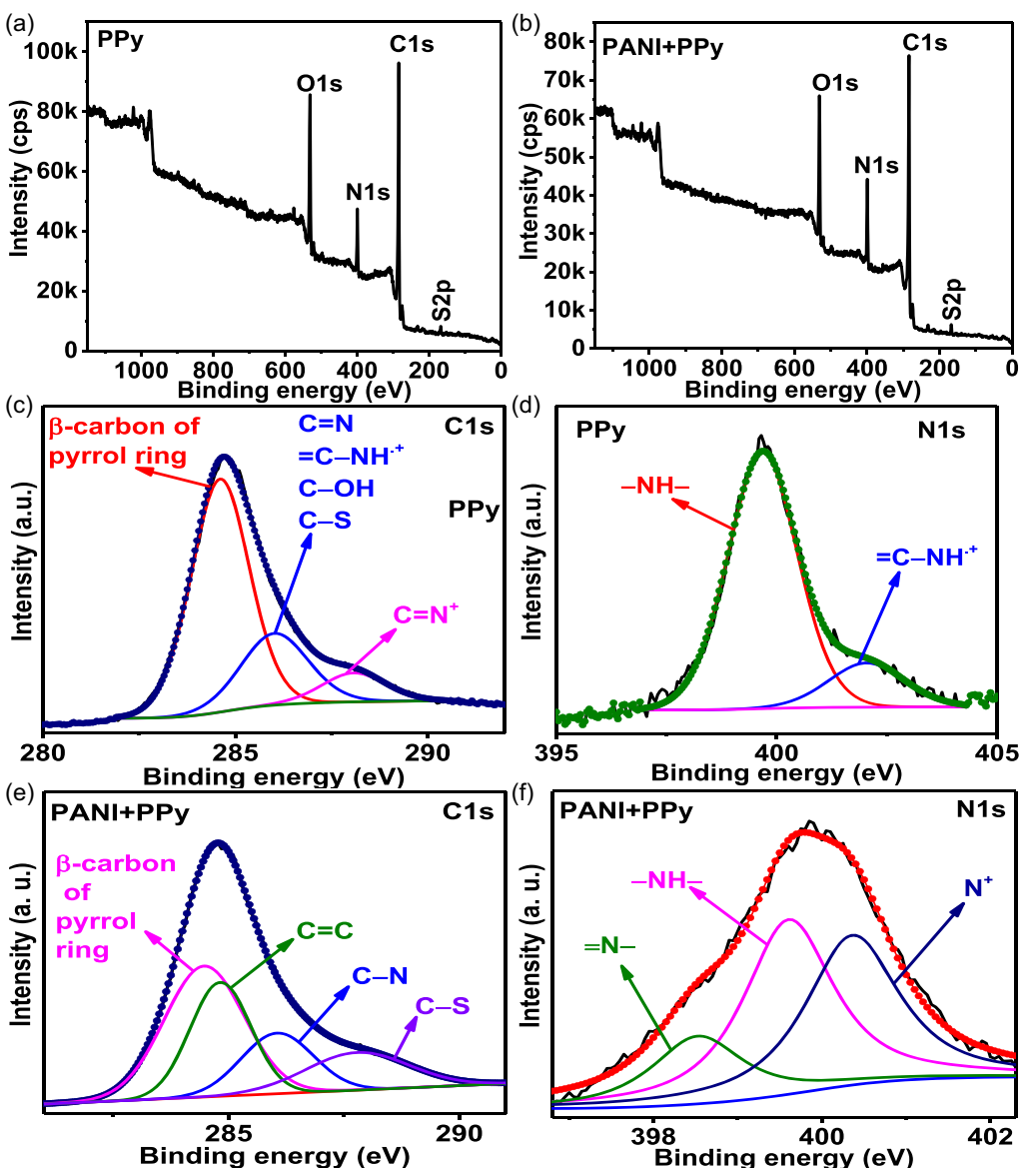


Figure 3. XPS a) survey spectrum b) C 1s, and c) N 1s core level spectra of PPy. XPS d) survey spectrum e) C 1s, and f) N 1s core level spectra of PANI + PPy.

3. Electrochemical Characterization

The CV (Figure 6a) and CD (Figure 6b) plots of PANI, PPy, and their composites of different weight compositions (PPs) have faradaic peaks and plateaus, indicating the faradaic mechanism of energy storage by them. The faradaic peaks seen in CV curves are due to the conversion of base form to salt form of PANI and PPy; faradaic transformation between leucoemeraldine to emeraldine form of PANI,^[24] and between oxidized and reduced forms of PPy.^[32] As seen in Figure 6a, the peaks at a lower potential region of 0 to ≈ 0.6 V majorly contribute to the energy storage, and faradaic area corresponding to that region is maximum for PANI and minimum for the PP composite of 1:1 ratio (PP(1:1)). As the amount of PPy in PANI increases, the faradaic area decreases and even the least weight ratio of 1:0.025 of PANI and PPy (PP(1:0.025)) exhibit lower faradaic area than that of PANI. This trend could be

comprehended considering the fact that the measure of the faradaic area is the measure of the quantity of energy stored. That is, the pristine PANI exhibits the highest energy storage, indicating its superior energy storage character in pristine form. When the PPy was introduced to PANI, the energy storage began to decrease and the least energy storage occurred when they were in an equal proportion. This is attributed to the point that the addition of PPy to PANI decreases the faradaic active surface area and increases the intrinsic resistance. However, with respect to the performance of PPy, the addition of PANI has significantly increased its energy storage ability. This reduction in faradaic active surface area is further substantiated by the FESEM results and BET surface area analyses. As is seen in Figure 4a, the morphology of the PPy is particles in nature (nearly 0D), while that of PANI is fibrous in nature (1D) (Figure 4c). When PANI and PPy are combined, the obtained morphology is particles, which is of PPy

Table 1. XPS peak positions and their respective chemical species.	
PPy	
Element	Binding energy (eV) and species
C 1s	284.6 (β -carbon of pyrrole ring), 286.01 ($\text{C}=\text{N}$, $=\text{C}-\text{NH}^+$, $\text{C}-\text{OH}$, and $\text{C}-\text{S}$), and 288.08 ($\text{C}=\text{N}^+$) ^[45]
N 1s	399.68 ($-\text{NH}-$), 402.04 ($=\text{C}-\text{NH}^+$) ^[45]
O 1s	531.24, 532.34 ($\text{C}-\text{OH}-\text{N}$), ^[45] 530.1 ($\text{S}=\text{O}$), ^[46] 533.57 ($\text{C}-\text{OH}$) ^[46]
S 2p	168.16 (S 2p3/2), ^[47] 170.57 (S 2p3/2) ^[48,49] of $\text{S}=\text{O}$ of MSA
PANI + PPy	
C 1s	284.49 ($\text{C}=\text{C}$), ^[50] 284.83 (β -carbon of pyrrole ring), ^[45] 286.06 ($\text{C}-\text{N}$), ^[45] 287.88 ($\text{C}-\text{S}$) ^[50]
N 1s	398.55 ($=\text{N}-$), 399.61 ($-\text{NH}-$), 400.38 (N^+) ^[24]
O 1s	531.5, 532.66 ($\text{C}-\text{OH}-\text{N}$), ^[45] 530.54 ($\text{S}=\text{O}$), ^[46] 533.96 ($\text{C}-\text{OH}$) ^[46]
S 2p	168.56 (S 2p3/2) ^[47] of $\text{S}=\text{O}$ of MSA

(Figure 4e). Similarly, the BET surface area of PANI is reduced when combined with PPy as seen above. The CD curves of PANI, PPy, and PPs at 1 A g^{-1} (Figure 6b) are with plateaus, indicating their faradaic energy storage character, and the maximum discharge time (t_d) is provided by the PANI (Figure S7, Supporting Information). With an increase in the quantity of PPy in PPs, the t_d decreases, indicating the point that the addition of PPy to PANI is negatively affecting the energy storage character of PANI. The CV and CD curves of PANI at different scan rates (Figure 6c) and current densities (Figure 6d), respectively, depict that the PANI exhibit better retention of Faradaic energy storage character and superior rate capability even up to 0.1 V s^{-1} and 18 A g^{-1} , which is due to its structural advantage of possessing a larger number of mesochannels in its structure, facilitating the effective diffusion of electrolytes even at high scan rates and current densities. The IR drops of PANI, PPy, PP(1:1), PP(1:0.4), PP(1:0.2), PP(1:0.05), and PP(1:0.025) obtained at 1 A g^{-1} are 0.25, 0.15, 0.26, 0.17, 0.28, 0.26, and 0.29 V, respectively. As the amount of PPy decreases in PPs, the IR drop increases, and the highest IR drop is provided by PP(1:0.025). Despite the relatively low IR drop of PPy, it provides lower energy storage, which is due to the lower surface area it offers, while the inverse is the case with PANI. Q (Equation S2, Supporting Information), E (Equation S3, Supporting Information), P (Equation S4, Supporting Information), and coulombic efficiency (η) (Equation S5, Supporting Information) of the PANI, PPy, and PPs are presented in Table 2. Table 2 depicts that the Q obtained from PANI, PPy, PP(1:1), PP(1:0.4), PP(1:0.2), PP(1:0.05), and PP(1:0.025) are 74.82, 12.24, 0.54, 33.04, 48.36, 58.24, and 72.14 C g^{-1} , respectively at 1 A g^{-1} . The maximum energy storage of PANI is due to its higher number of redox transformations in relation to PPy. Therefore, as the amount of PANI increases, the Q increases, and the inverse happens when the amount of PPy increases. As is seen in Table 2, the Q exhibited by the pristine PPy is 12.24 C g^{-1} , while that of PP(1:0.4), PP(1:0.2), PP(1:0.05), and PP(1:0.025) are higher than that of pristine PPy. Therefore, the addition of PANI to PPy increases its energy storage. On

the other hand, the Q exhibited by the pristine PANI is 74.82 C g^{-1} , while that of PP(1:0.4), PP(1:0.2), PP(1:0.05), and PP(1:0.025) are lower than PANI; therefore addition of PPy to PANI decreases the energy storage of PANI. These observations are well supported by the FE-SEM and BET results discussed above. As shown in Figure 7a, the PANI exhibits a high Q , but the better rate capability is exhibited by PP(1:0.025). That is, the presence of PPy in a minimal amount aids the improvement of rate capability and sustainability to a high current of PANI. The maximum applied current density that PANI, PPy, PP(1:1), PP(1:0.4), PP(1:0.2), PP(1:0.05), and PP(1:0.025) withstand are 18, 8, 2, 14, 15, 15, and 28 A g^{-1} , respectively. The % retention of Q at a common current density of 8 A g^{-1} are 45.97, 31.37, 35.83, 33.74, 44.78, and 54.78 % for PANI, PPy, PP(1:0.4), PP(1:0.2), PP(1:0.05), and PP(1:0.025), respectively. The rate capability of PP(1:1) was not mentioned as it lasts only up to 2 A g^{-1} . The percentage retentions of Q of PANI and PP(1:0.025) at 18 and 28 A g^{-1} are 9.14 and 18.63%, respectively. This higher rate capability furnished by the minimal amount of PPy with PANI in PP(1:0.025) is attributed to the combined play of good electrical conductivity of PPy, as well as the larger surface area and higher porosities offered by PANI. In addition, the high rate capability of PP(1:0.025) is substantiated as follows:

The CV plots of PANI, PPy, and PP(1:0.025) at different scan rates are shown in Figure S8a, S8b and S8c, Supporting Information, respectively, and the plots of the anodic peak current (i_{pa}) versus $i_{pa}/\sqrt{\text{scan rate}}$, $\log i_{pa}$ versus log scan rate, and $i_{pa}/\sqrt{\text{scan rate}}$ versus $\sqrt{\text{scan rate}}$ derived from them are also shown in Figure S8d, S8e, and S8f, Supporting Information, respectively. The diffusion coefficient (D_o) values attained from the plots of i_{pa} versus $\sqrt{\text{scan rate}}$ using the Randles-Sevcik equation^[37] (Equation S6, Supporting Information) are 0.0066 and $0.00932 \text{ cm}^2 \text{s}^{-1}$ for PANI and PP(1:0.025), respectively. The b-values (Equation S7, Supporting Information) attained from the plots of $\log i_{pa}$ versus log scan rate are 0.6825 and 0.8225 for PANI and PP(1:0.025), respectively. The percentage of the diffusion-controlled intercalation process and surface capacitive processes (EDLC + surface redox reaction) (Equation S8 and S9, Supporting Information) determined from the plots of $i_{pa}/vs\sqrt{\text{scan rate}}^{[37-39]}$ are 90.84 and 9.16% for PANI, and 74.71 and 25.29% for PP(1:0.025), respectively.

It is evident from the attained D_o that the addition of a small percentage of PPy to PANI has increased its diffusion coefficient. Because of this, the PP(1:0.025) exhibits a higher rate capability than PANI. However, it is to be remarked that at lower scan rates, the PANI produces higher i_{pa} than PP(1:0.025), but with an increase in the scan rate, the i_{pa} of PANI decreases when compared to that of the PP(1:0.025), which is attributed to the higher D_o of PP(1:0.025). Another observation that supports the higher rate capability of PP(1:0.025) over PANI is their b-values. The b-value of PP(1:0.025) (0.8225) is in between the values of 1 and 0.5, indicating the occurrence of a combination of a diffusion-controlled intercalation process (bulk process) and surface capacitive processes (EDLC + surface redox reaction), while that of PANI is closer to 0.5 (0.6825), indicating the major occurrence of a diffusion-controlled intercalation process.^[37] The kinetics

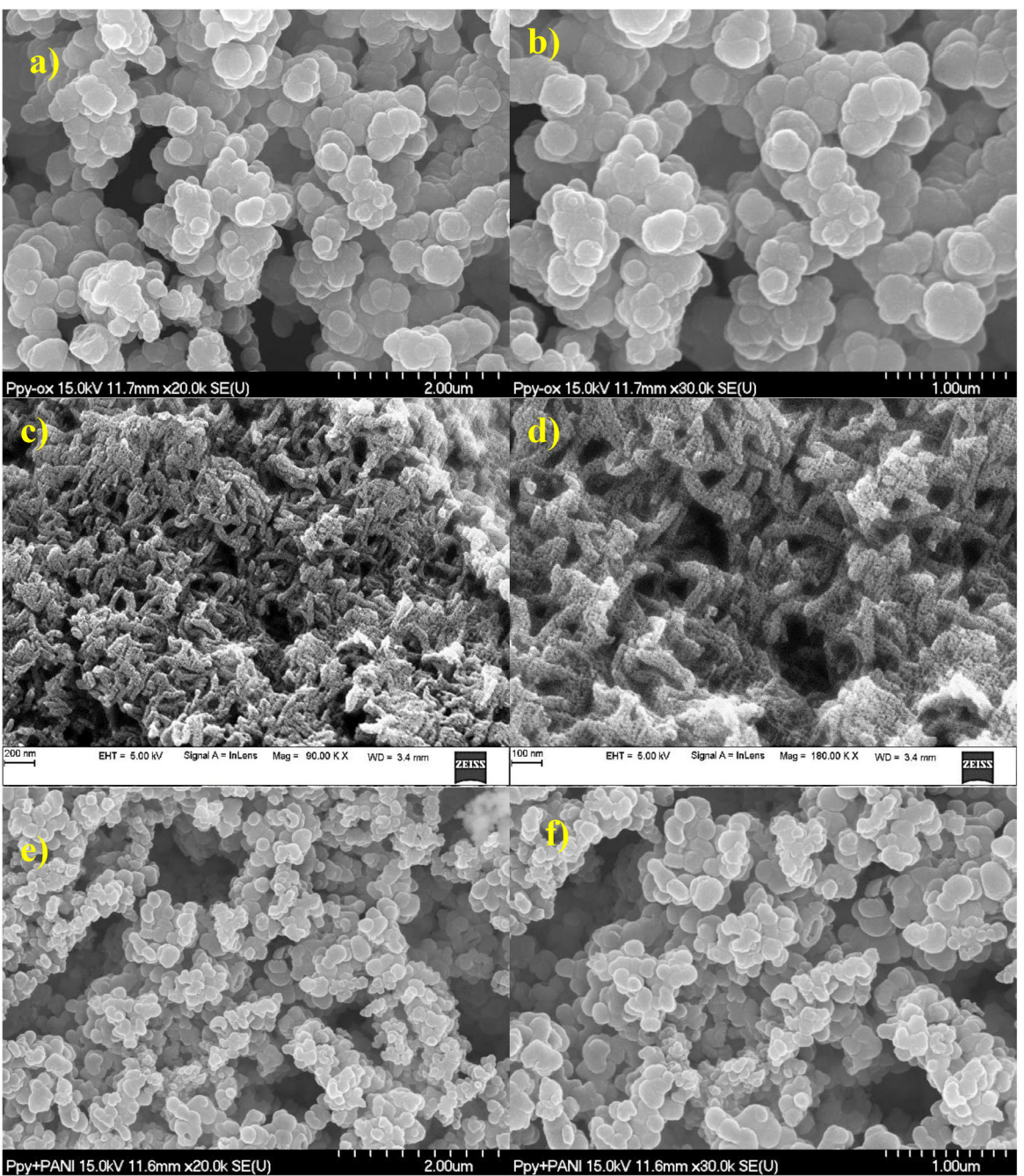


Figure 4. FESEM images of a,b) PPy; c,d) PANI; and e,f) PANI + PPy.

of the surface capacitive process is higher than that of the bulk processes; therefore, at higher scan rates, the PP(1:0.025) maintains a similar level of energy storage process as it does at lower scan rates, while the PANI fails to do it as it majorly involves the bulk process of a diffusion-controlled intercalation process. Yet, another observation that supports the observation of a higher rate capability of PP(1:0.025) is the percentage occurrence of surface and bulk energy storage processes, that is the addition of a small amount of PPy to PANI increases the extent of the surface energy storage process from 9.16 to 25.29%. This increased surface energy storage process increases the rate capability of

PP(1:0.025) higher than the PANI. Since the CV curves of PPy did not produce a significant faradaic curve, their D_{or} , b-values, and percentage contribution to the surface- and diffusion-controlled energy storage processes were not deduced.

The E attained at a P of 0.6 kW kg^{-1} (1 A g^{-1}) (Figure 7b) of PANI, PPy, PP(1:1), PP(1:0.4), PP(1:0.2), PP(1:0.05), and PP(1:0.025) are 12.47, 2.04, 0.09, 5.51, 8.06, 9.71, and 12.02 Wh kg^{-1} , respectively. The PANI, PPy, and PPs retain their E with an increase in current density with a similar trend as observed in the case of retention of their Q . The η (Figure 7c) exhibited by PANI, PPy, PP(1:1), PP(1:0.4), PP(1:0.2), PP(1:0.05), and PP(1:0.025) at 1 A g^{-1}

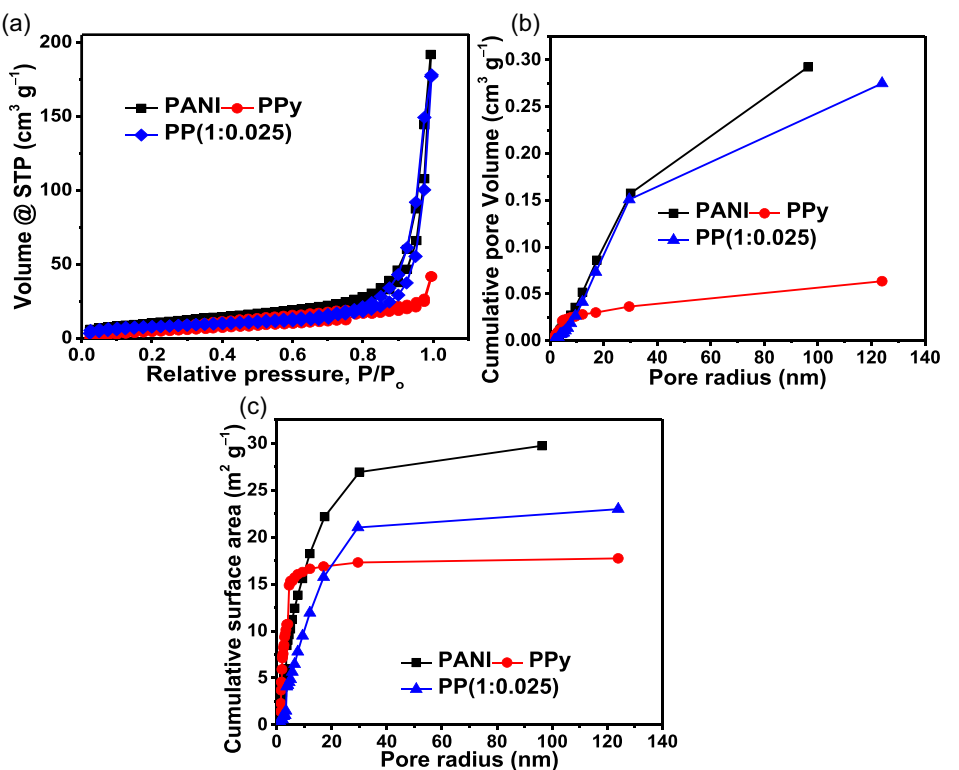


Figure 5. a) BET isotherm plots, b) plots of cumulative pore volume versus pore radius, and c) cumulative surface area versus pore radius of PANI, PPy, and PP(1:0.025).

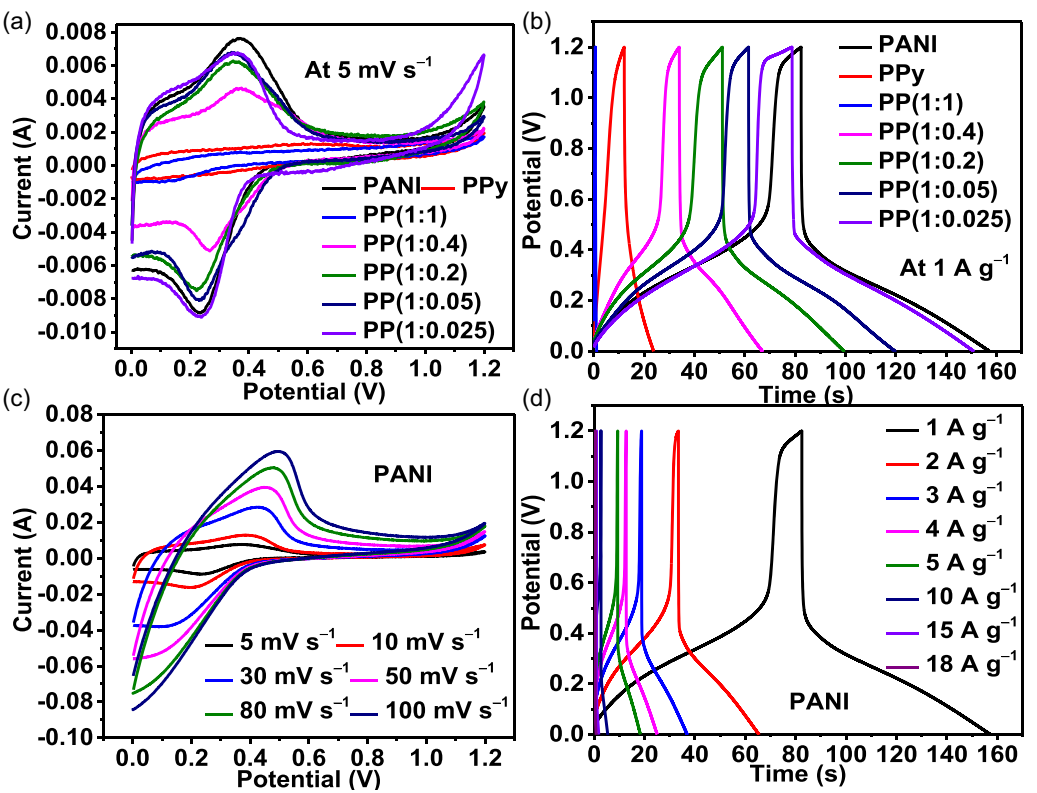


Figure 6. a) CV plots and b) CD plots of PANI, PPy, and their composites of different weight compositions. c) CV curves at different scan rates, and d) CD curves at different current densities of PANI.

Table 2. Energy storage parameters of PANI, PPy, and PP at 1 a g⁻¹.

Electrolytes	Q [C g ⁻¹]	E [Wh kg ⁻¹]	P [kW kg ⁻¹]	η [%]
PANI	74.82	12.47	0.6	93.57
PPy	12.24	2.04	0.6	90.77
PP(1:1)	0.54	0.09	0.6	84.37
PP(1:0.4)	33.04	5.51	0.6	97.17
PP(1:0.2)	48.36	8.06	0.6	94.60
PP(1:0.05)	58.24	9.71	0.6	94.66
PP(1:0.025)	72.14	12.02	0.6	91.50

are 93.57, 90.77, 84.37, 97.17, 94.60, 94.66, and 91.50%, respectively. The addition of PPy to PANI nor the PANI to PPy has not brought about significant changes in the η, which indicates the

occurrence of faradaic reaction with a similar rate in both PANI, PPy, and their composites. The η ascends with an increase in current density, close to 100% in all cases of the electrodes.

The evaluation of the cyclic stability of PPy and PP(1:0.025) was conducted at the scan rate of 0.4 V s⁻¹ for 5000 cycles (Equation S10, Supporting Information). The cyclic stability of PANI has already been studied thoroughly and presented in our previous work.^[24] The plots of the percentage retention of Q versus number of cycles are depicted in Figure 7d. The PPy and PP(1:0.025) retain 35.87 % and 43.96 % of their initial Q at the end of 5000 cycles. The poor cyclic stability of PPy and PP(1:0.025) is due to the larger volumetric swelling and contraction that they undergo during energy storage and delivery processes.^[11] In addition, the poorer cyclic stability of PPy indicates its higher extent of structural degradation in relation to PP(1:0.025).

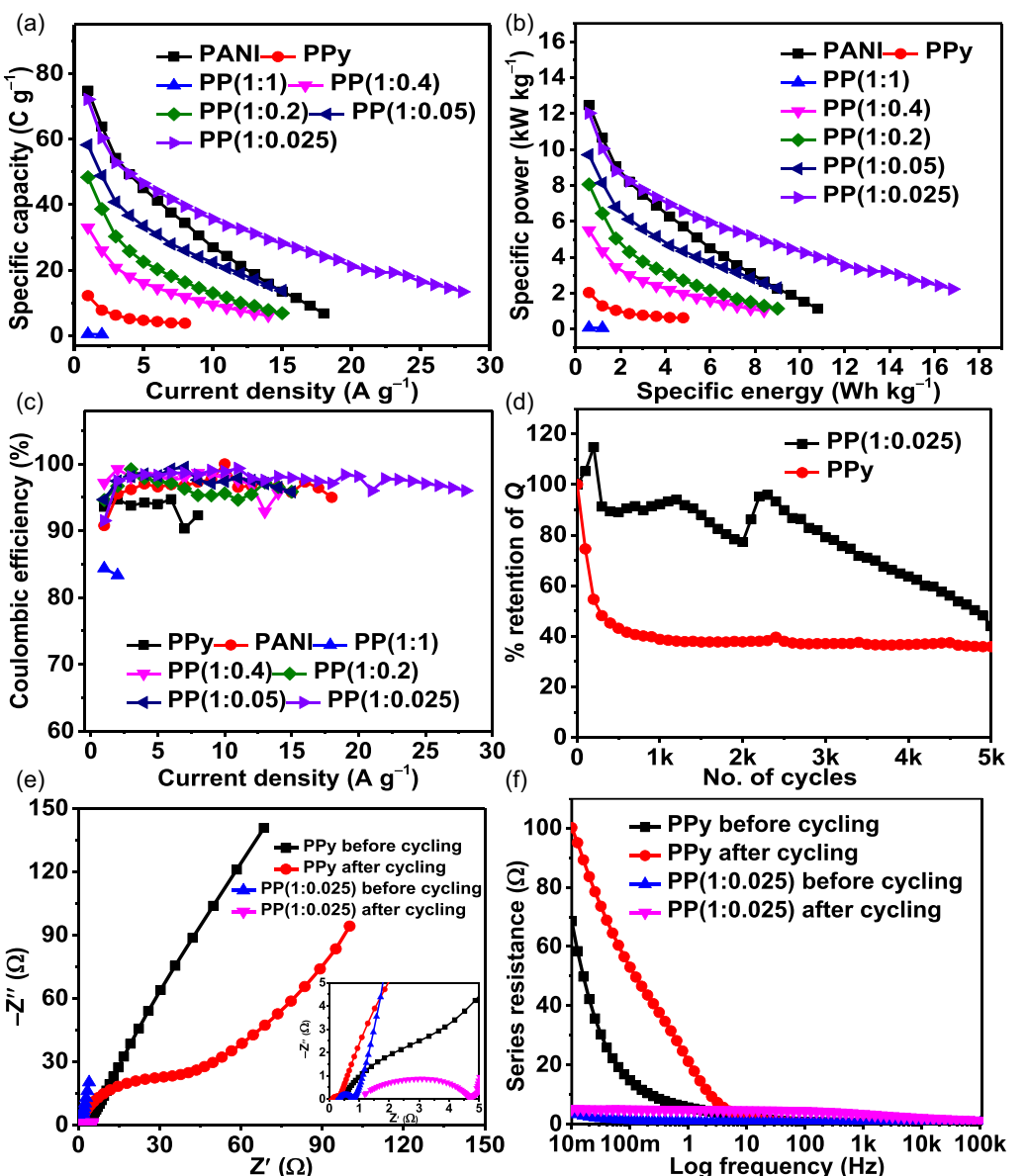


Figure 7. Plots of a) Q versus current density, b) P versus E, and c) η versus current density of PANI, PPy, and their composites of different weight compositions. d) Plots of percentage retention of Q versus number of cycles, e) Nyquist plots of PPy and PP(1:0.025) before and after cycling, and f) plots of series resistance versus log frequency.

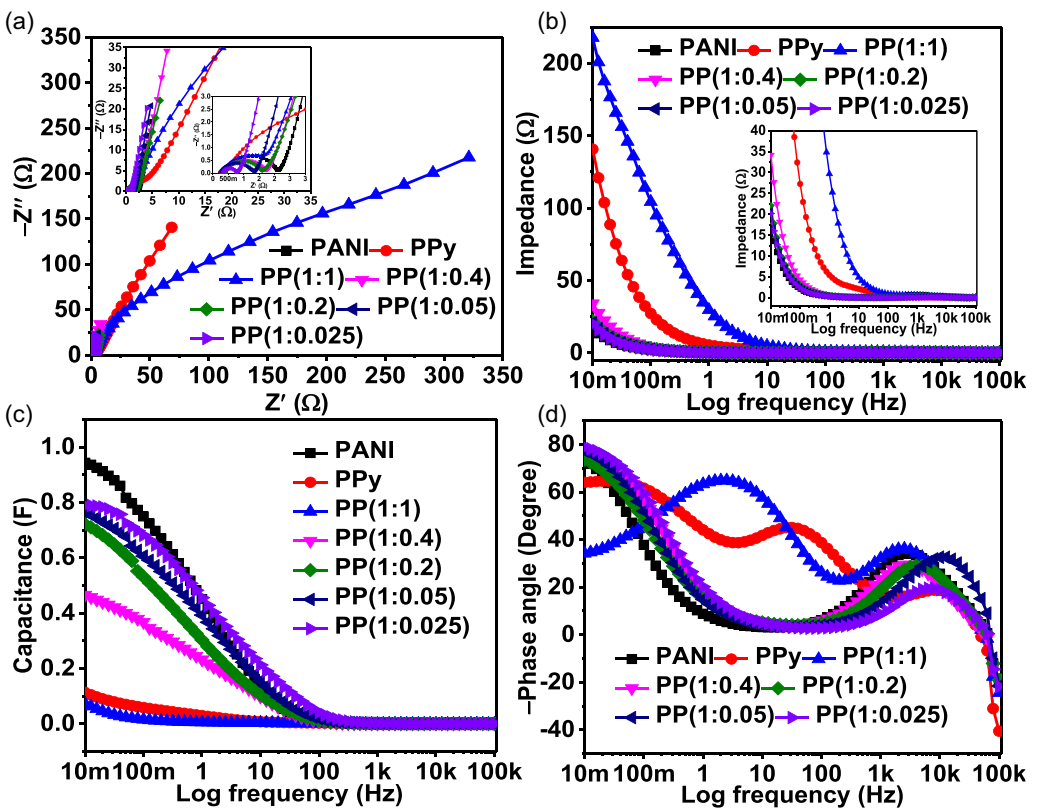


Figure 8. a) Nyquist plots, b) Bode impedance plots, c) plots of capacitance versus log frequency, and d) Bode phase angle plots of PANI, PPy, and their composites of different weight compositions.

In addition, the Nyquist plots and the plots of series resistance versus log frequency obtained before and after 5000 cycles of PPy and PP(1:0.025) are depicted in Figure 7e. As shown, the series resistance, which is the combination of different resistances that are involved in the energy storage processes, increased after 5000 cycles for both PPy and PP(1:0.025), indicating the structural degradations that they have undergone during continuous charging and discharging of the cyclic stability test. The series resistances (Figure 7f) obtained at a lower frequency of 0.01 Hz are 68.49 and 100.12 Ω for PPy before and after 5000 cycles, respectively, and 3.96 and 5.12 Ω for PP(1:0.025) before and after 5000 cycles, respectively.

The Nyquist plots of PANI, PPy, and PPs (Figure 8a) possess semicircles at higher frequencies and Warburg line at lower frequencies, indicating their capacitive natures. The Bode impedance (Figure 8b) of PANI, PPy, PP(1:1), PP(1:0.4), PP(1:0.2), PP(1:0.05), and PP(1:0.025) at 0.01 Hz are 16.87, 140.7, 217.7, 34.16, 22.06, 20.78, and 20.18 Ω , respectively. The least impedance is exhibited by the PANI, and with an increase in the amount of PPy, the impedance increases. The plots of capacitance versus log frequency (Figure 8c) have exhibited the contrary characters of plots impedance versus log frequency. That is, the maximum capacitance is provided by PANI, and with an increase in the amount of PPy in PPs, the capacitance decreases. The capacitance

Table 3. Comparison of achieved energy storage parameters of PANI and PP(1:0.025) with similar composites.

Composite	Electrolyte	E [V]	E [W h kg ⁻¹]	P [kW kg ⁻¹]	Cyclic stability	Ref.
2-EL system						
PANI-PPy copolymer // N-doped activated carbon	1 M H ₂ SO ₄	1.6 V	31.9 at 1 A g ⁻¹	0.8114	–	[51]
Poly(aniline-co-pyrrole)	PVA/H ₂ SO ₄ hydrogel	1 V	22.00	0.125	79.9% retention after 1000 cycles at 3 A g ⁻¹	[52]
Phytic acid doped poly(aniline-co-pyrrole)	1 M H ₂ SO ₄	1 V	12.2	0.500	–	[53]
Present work PANI	1 M H ₂ SO ₄	1.2 V	12.47 at 1 A g ⁻¹	0.600	–	–
Present work PANI-PPy (1:0.025)	1 M H ₂ SO ₄	1.2 V	12.02 at 1 A g ⁻¹	0.600	43.96 % retention up to 5000 cycles at 0.4 V s ⁻¹	–

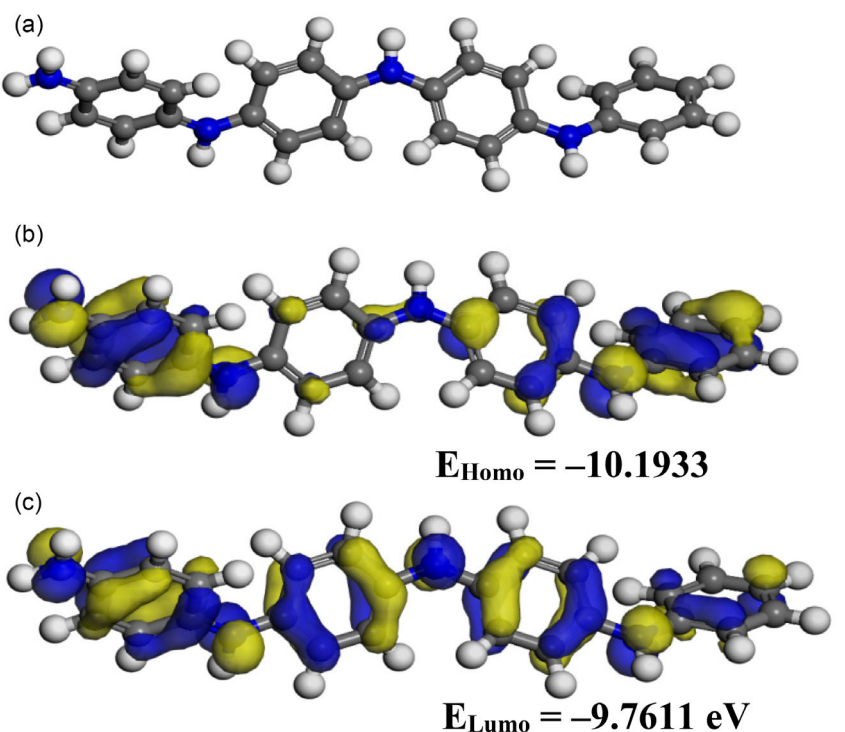


Figure 9. a) FMOT, b) HOMO, and c) LUMO of protonated PANI.

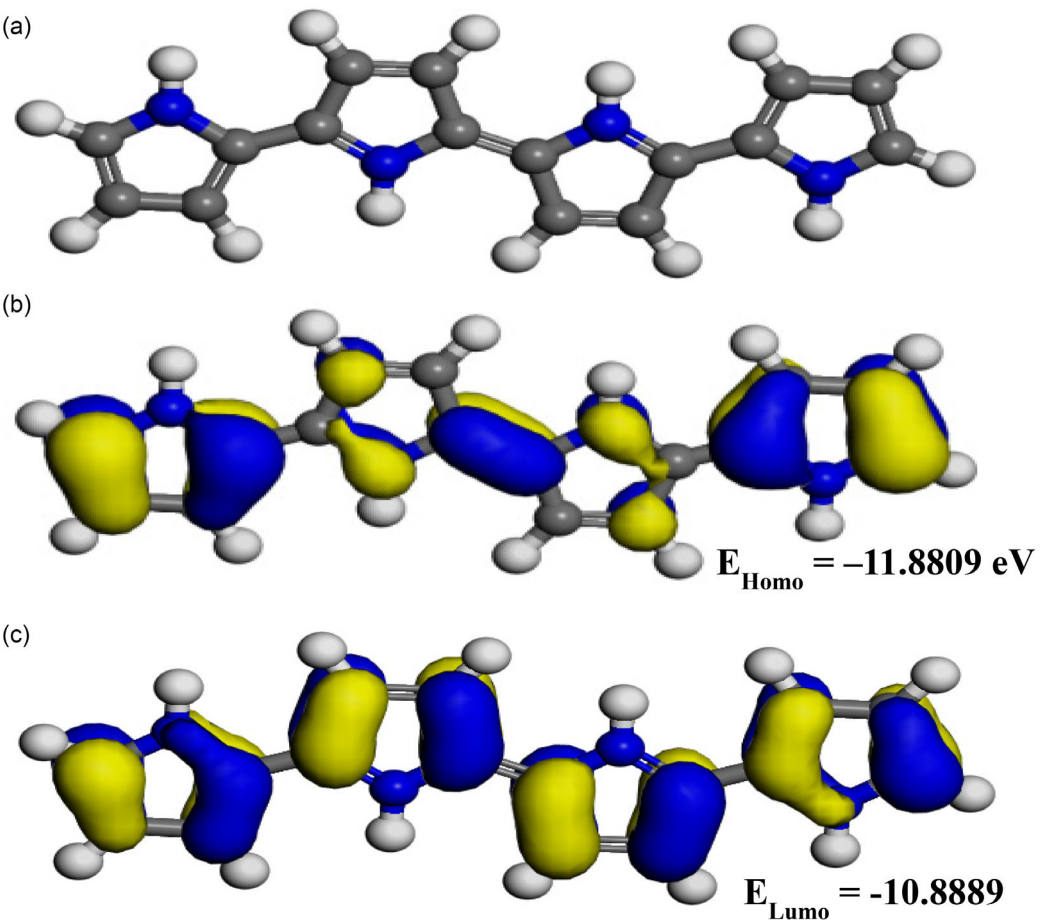


Figure 10. a) FMOT, b) HOMO, and c) LUMO of protonated PPy.

(Equation S11, Supporting Information) obtained at 0.01 Hz from PANI, PPy, PP(1:1), PP(1:0.4), PP(1:0.2), PP(1:0.05), and PP(1:0.025) are 0.9434, 0.1131, 0.0731, 0.4658, 0.7213, 0.7655, and 0.7886 F, respectively. The Bode plots (Figure 8d) of PANI, PPy, and PPs do not reach -90° at lower frequencies but at lower than -80° , which indicates that the electrode materials are not perfect capacitors; instead, they are deviated capacitors, and the direction towards which the plots are moving at lower frequencies is taking them towards faradaic supercapacitors or supercapattery. The relaxation time (τ) (Equation S12, Supporting Information) of PANI, PPy, PP(1:1), PP(1:0.4), PP(1:0.2), PP(1:0.05), and PP(1:0.025) are 0.8509, 0.1312, 0.8190, 0.6408, 0.7614, 0.7129, and 0.5978 s, respectively. The maximum energy storage of PANI is reflected in its high τ . The obtained performances of PANI and PP(1:0.025) are comparable with the performances reported for the copolymers of PANI and PPy, as seen in Table 3.

4. DFT Analyses

The frontier molecular orbitals (FMO), HOMO, and LUMO of the protonated or acid-doped PANI (Figure 9a–c), protonated PPy

(Figure 10a–c), unprotonated PANI (Figure 11a–c), and unprotonated PPy (Figure 12a–c), respectively, are utilized to deduce the energy gap (ΔE_{gap}) (bandgap) (Equation S13, Supporting Information)^[40] between the HOMO and LUMO of the protonated PANI, protonated PPy, unprotonated PANI, and unprotonated PPy. The E_{gap} of protonated PANI, protonated PPy, unprotonated PANI, and unprotonated PPy are 0.432, 0.992, 1.202, and 1.172 eV, respectively. These magnitudes indicate that the protonated PANI and PPy possess a lower bandgap than that of unprotonated ones and the protonated PANI possesses a lower bandgap than that of protonated PPy. The synthesized PANI, PPy, and PPs are protonated. The lower bandgap of PANI indicates its higher conductivity than PPy. In addition, both the PANI^[41] and PPy^[42] are similar types of semiconductors (P-type). Therefore, the electrostatic interaction between them could be minimal and thus, their combination could be unsuccessful in complementing each other. The addition of low conductive PPy to PANI would reduce the conductivity of PANI and thus, reduce its energy storage performance. These theoretical studies support the experimental data obtained. Further, even in an unprotonated form, the PANI has lower bandgap and higher conductivity than PPy as the DFT studies indicate.

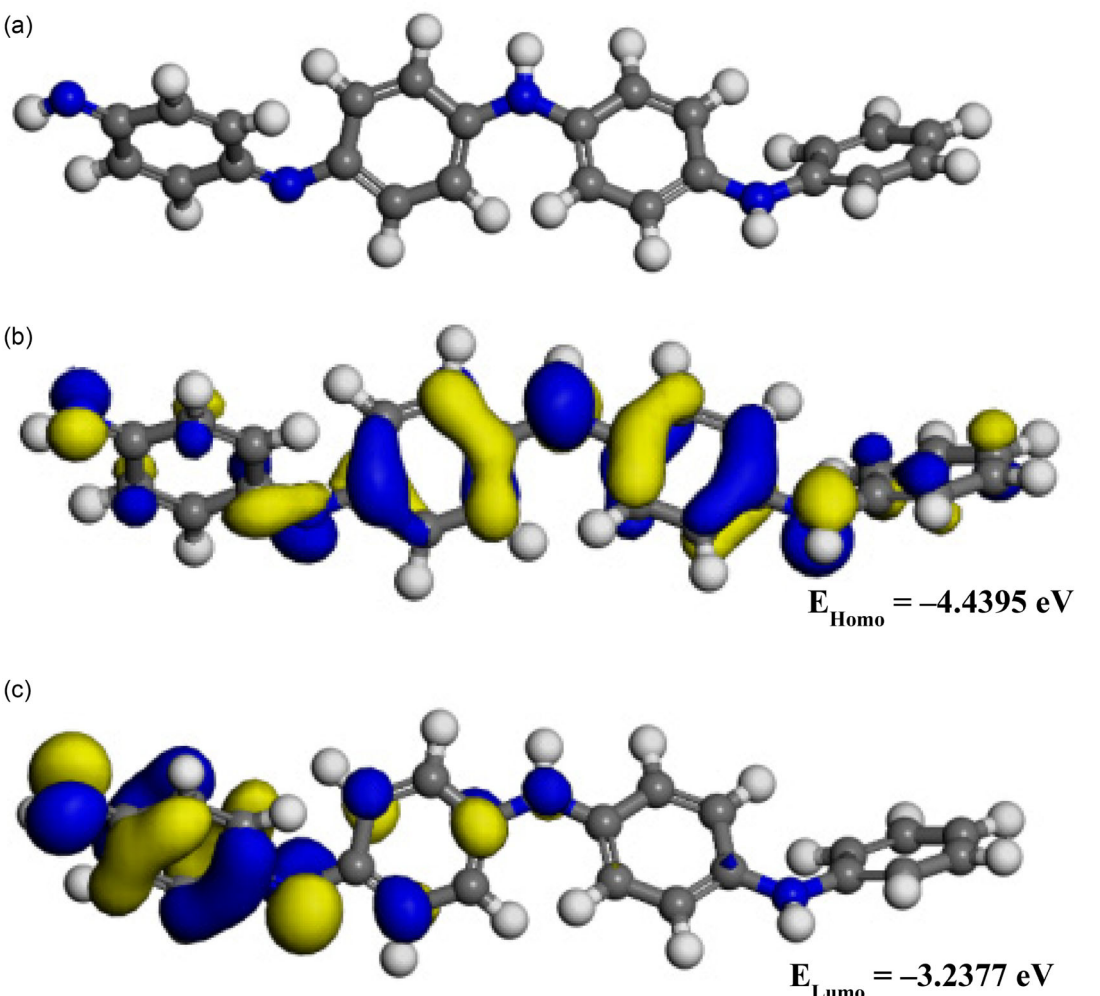


Figure 11. a) FMOT, b) HOMO, and c) LUMO of unprotonated PANI.

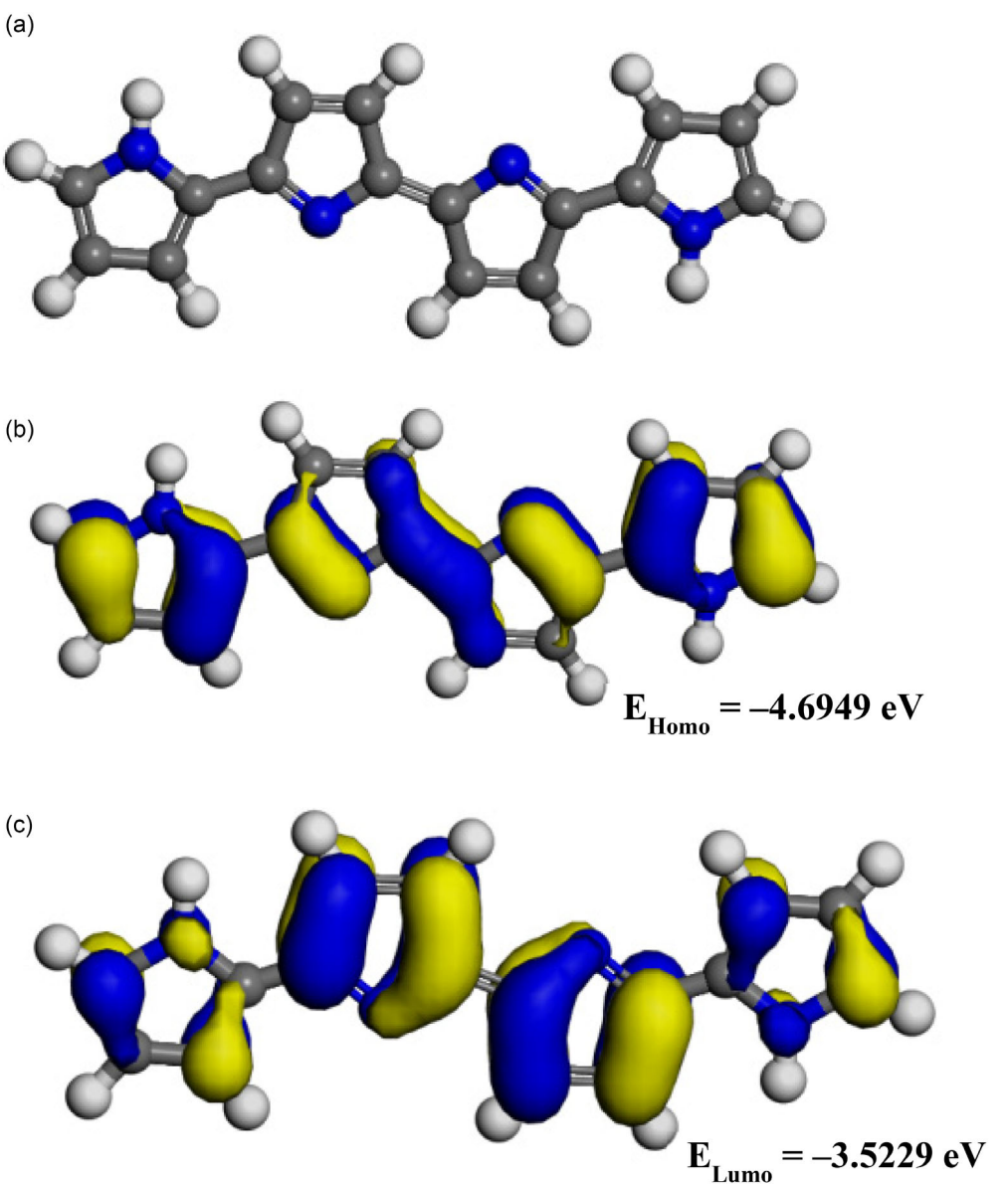


Figure 12. a) FMOT, b) HOMO, and c) LUMO of unprotonated PPy.

As it is seen from **Table 4** and in **Figure 13a-d**, all the nitrogen atoms and carbon atoms that are involved in the π -bonding are with negative Mulliken charges. The carbon atoms that are in the α -position to the nitrogen have positive charges in PANI and PPy. The negative charges of the nitrogen atoms indicate their high electronegativity and that of carbon involved in the π -bonding indicate the high electron density on them due to the π electron

cloud. The positive charges of the carbon atoms that are in the α -position to the nitrogen atoms indicate the withdrawal of its electron density by nitrogen atoms. Since the nitrogen atoms of both the PANI and PPy are with negative charges with the least of differences in values, the interaction between them is less possible. Therefore, the combination of them is least expected to produce any electrostatic synergistic interactions. It is important to

Table 4. Mulliken charges on different atoms of PANI and PPy.

Material	N1	C1	C2	C3	C4	C5	C6	N2	N3	N4
Protonated PANI	-0.317	0.232	-0.083	-0.096	0.179	-0.065	-0.078	-0.279	-0.284	-0.288
Protonated PPy	-0.278	0.228	-0.095	-0.052	0.133	-	-	-0.342	-0.342	-0.287
Unprotonated PANI	-0.377	0.131	-0.084	-0.042	0.115	-0.098	-0.051	-0.288	-0.346	-0.367
Unprotonated PPy	-0.298	0.201	-0.111	-0.097	0.060	-	-	-0.376	-0.376	-0.298

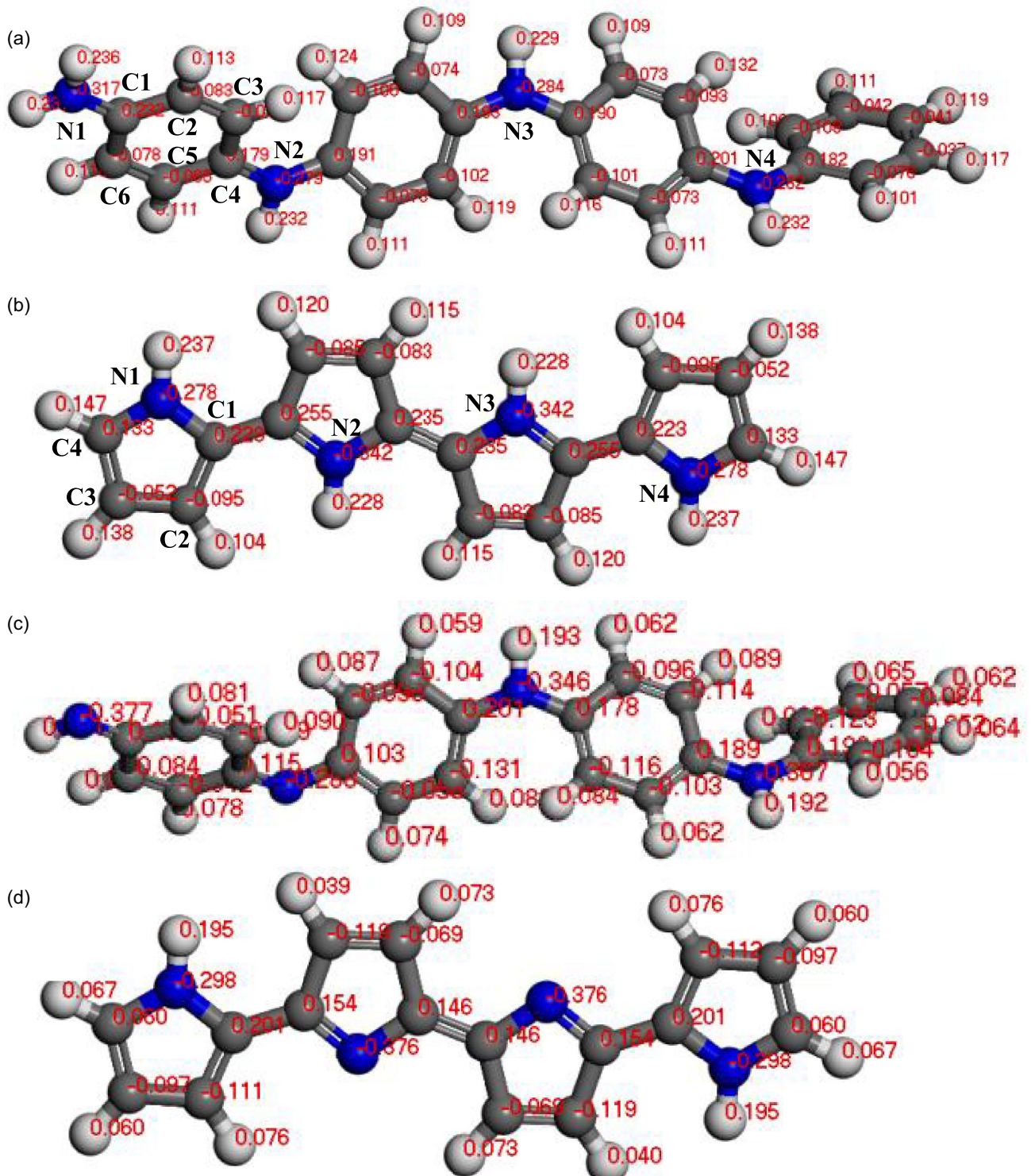


Figure 13. Distribution of Mulliken charges on the atoms of a) protonated PANI, b) protonated PPy, c) unprotonated PANI, and d) unprotonated PPy.

note that the negative charges on the nitrogen atoms of the protonated PANI and PPy are lesser than those in the unprotonated ones. This reduction in negative charge indicates the addition of proton onto the nitrogen atoms during doping and the mobilization of its electron density to the added proton during doping.

In the molecular surface electrostatic potential (ESP) maps (Figure 14) of PANI and PPy, the blue-colored regions indicate the electron-poor regions, the red colored regions indicate the electron-richer regions, and the yellow-colored regions indicate the regions with intermediate electron density. The red regions are seen on the electronegative nitrogen atoms and on the π

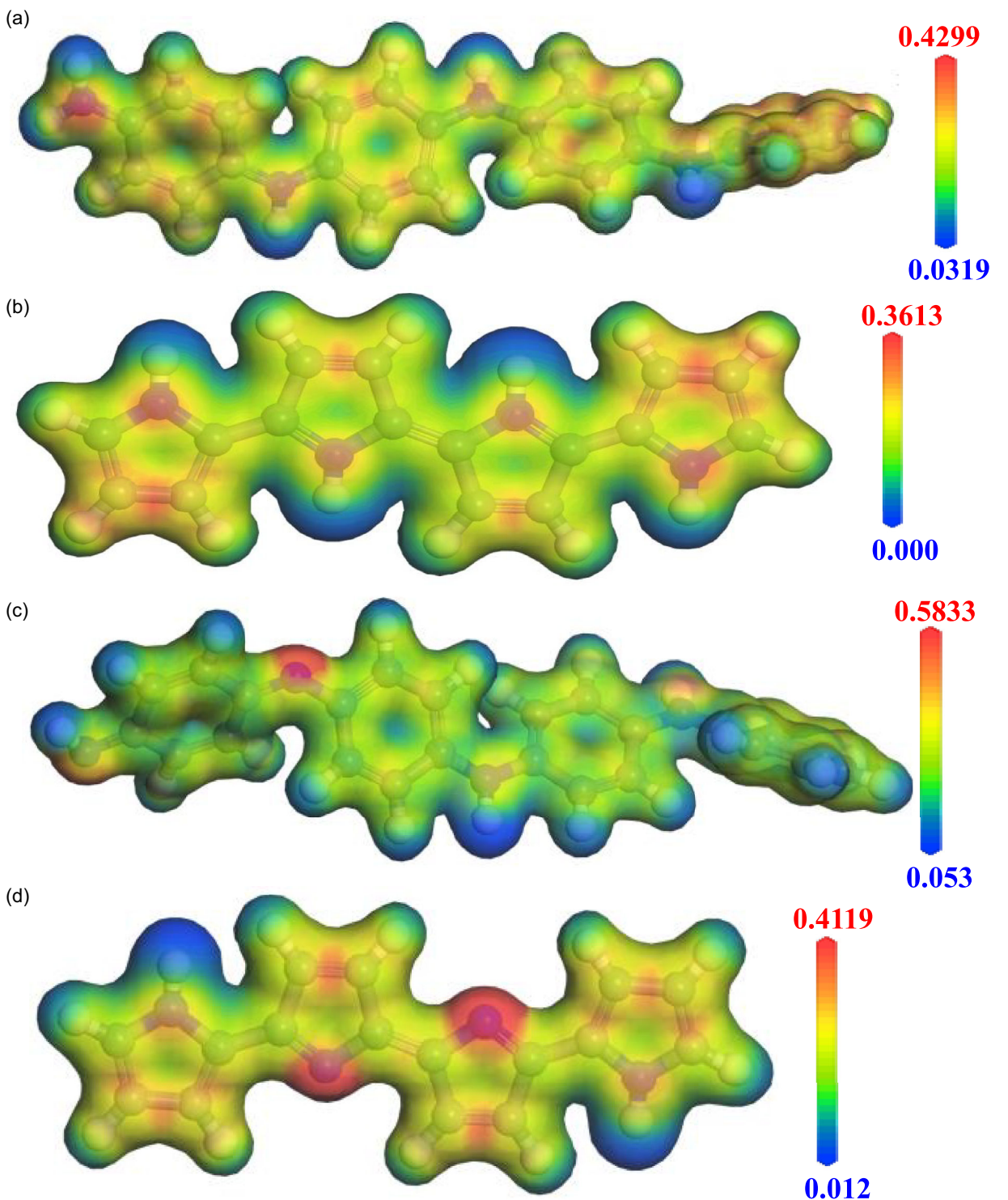


Figure 14. Molecular surface ESP mappings of a) protonated PANI, b) protonated PPy, c) unprotonated PANI, and d) unprotonated PPy.

bonds. The blue regions are seen on the hydrogen atoms. The yellow regions are seen along the backbone of the polymers, which indicate the continuous delocalization of π electrons along the polymer chain. The relatively bright yellow regions on the protonated PANI (Figure 14a) and protonated PPy (Figure 14b) than that in the unprotonated PANI (Figure 14c) and unprotonated PPy (Figure 14d) indicate the effective delocalization of

electrons on their backbones when compared to that in the unprotonated PANI and PPy. This effective delocalization provides lower bandgaps and higher conductivities to the protonated PANI and PPy than those of unprotonated PANI and PPy.^[43]

The global indices^[44] of reactivity such as ionization potential (I in eV) (Equation S14, Supporting Information), electron affinity (A in eV) (Equation S15, Supporting Information), electrophilicity

Table 5. Ionization energy, electron affinity, chemical potential, hardness, softness, and electrophilicity of protonated PANI, protonated PPy, unprotonated PANI, and unprotonated PPy obtained from DFT analysis.

Material	Ionization energy [I] [eV]	Electron affinity [A] [eV]	Electrophilicity [ω] [eV]	Hardness [H] [eV]	Softness [S] [eV $^{-1}$]
Protonated PANI	10.1933	9.7611	230.3204	-9.9772	2.3137
Protonated PPy	11.8809	10.8889	130.6612	-11.3849	1.0081
Unprotonated PANI	4.4395	3.2377	12.2606	-3.8386	0.8321
Unprotonated PPy	4.6949	3.5229	14.4053	-4.1089	0.8532

(ω in eV) (Equation S16, Supporting Information), hardness (H in eV) (Equation S17, Supporting Information), and softness (S in eV $^{-1}$) (Equation S18, Supporting Information) were calculated from the DFT results and are presented in **Table 5**. As shown in Table 5, the ionization energy increases after doping. These high ionization energies of protonated PANI and PPy indicate the chemical stability and difficulties involved in removing an electron from molecular orbitals of protonated PANI and PPy. This high ionization energy is due to the lower negative Mulliken charges on the nitrogen atoms of protonated PANI and PPy. This is due to the reason that during the doping the lone pair of electrons available on the nitrogen is used to form a bond with the hydrogen that comes from acidic dopants. Because of this, that is the nitrogen loses its electron density, the increase in the overall ionization energy of protonated PANI and PPy is observed. In addition, the same loss of electron density by nitrogen increases the overall electron affinities of protonated PANI and PPy than that of unprotonated ones. Further, this loss of the lone pair of electrons of nitrogen creates lower electron density on the polymer backbone, which increases the ω of the protonated PANI and PPy than that of the unprotonated ones. The higher values of ω of the protonated PANI and PPy indicate the effective doping of protons on their backbones.^[43] The H and S are used to gauge the stability and reactivity of molecules.^[43] As the softer molecules tend to easily donate electrons to the acceptors, they are more reactive. In addition, the softer molecules tend to have lower bandgaps and harder molecules tend to have higher bandgaps.^[43] The S order of the protonated and unprotonated PANI and PPy are in concordance with the order of their bandgaps. The highest S and lowest bandgap are attained for protonated PANI, indicating its high conductivity, effective delocalization of the π -electrons and high reactivity to undergo transformation between its redox forms.

5. Conclusion

The PANI and PPy were experimented for their synergy in improving their energy storage property in the form of symmetric supercapacitors using an aqueous acidic electrolyte of 1 M H₂SO₄. The results of the energy storage study reveal that no synergy was established, nor was an increase in PANI's energy storage attained. Instead, a decrease in energy storage of PANI was attained when combined with PPy. The conductivity and surface area of PANI are reduced when composited with PPy. However, the addition of a minimal amount of PPy to PANI significantly increases the PANI's rate capability, with a slight decrease in

its energy storage. In addition, the addition of PANI to PPy increases the energy storage of the PPy to a larger extent. Therefore, it would be of a negative notion to combine PANI and PPy to increase their overall energy storage. However, it is clear that the addition of PANI to PPy increases the energy storage of PPy and not vice versa. The obtained Q , E , P , and η of PANI are 74.82 C g $^{-1}$, 12.47 W h kg $^{-1}$, 0.6 kW kg $^{-1}$, and 93.57 %, respectively. The negative synergy between PANI and PPy in storing energy is observed from the study, and it is substantiated that PANI stores higher energy individually than it does in combination with PPy. Therefore, it is beneficial not to add PPy with PANI for energy storage purposes; instead, the addition of PANI with faradaic metal oxides and metal hydroxides would be beneficial as there is abundant literature available proving the synergy of metal oxide and hydroxides with PANI.

6. Experimental Section

Synthesis of Polyaniline

In the synthesis of PANI,^[24] 300 μ L of aniline was taken in 100 mL of distilled water (DW) in a beaker, stirred for 10 min for uniform mixing, 1.2 g of ammonium persulfate (APS) dissolved in a minimum amount of DW was added and followed by the addition of 10 mL of 3 M methanesulphonic acid (MSA) to the reaction mixture. The polymerization was continued for 5 h, then the obtained green color PANI was isolated and used for the analyses.

Synthesis of Polypyrrole

The PPy was synthesized by following the same procedure as mentioned in the synthesis of polyaniline, with the exception of using 300 μ L of pyrrole instead of aniline.

Synthesis of Polyaniline and Polypyrrole Composite

The composites of PP were synthesized by taking the mixtures of aniline and pyrrole in definite amounts to obtain them in different weight compositions. As an example, the synthesis of PP(1:1) is as follows.

In the synthesis of PP(1:1), 300 μ L of each of aniline and pyrrole were taken in 100 mL of DW in a beaker and stirred for 10 min for their uniform mixing. 2.4 g of APS dissolved in a minimum amount of DW was added, followed by the addition of 10 mL of 3 M MSA to the reaction mixture. The polymerization was continued for 5 h, and then the obtained green color PP(1:1) was isolated and used for the analyses. Similarly, PP composites of different weight compositions of 1:0.4, 1:0.2, 1:0.05, and 1:0.025 were synthesized and named as PP(1:0.4), PP(1:0.2), PP(1:0.05), and PP(1:0.025), respectively. The videograph of the synthesis of PANI and PPy is presented in Video S1.

The fabrication details (Figure S1, Supporting Information) and the characterization details of these PP composites as symmetric supercapacitors are provided in Section S1 and S2 of the supporting information.

Acknowledgements

A.V. acknowledges the financial support provided by the Science and Engineering Research Board (SERB), India, in the form of a National Post-Doctoral Fellowship (PDF/2023/000769). V.A. acknowledges financial support from the Anusandhan National Research Foundation (ANRF), Govt. of India, through Swarnajayanti Fellowship (SB/SJF/2020-21/12).

Conflict of Interest

The authors declare no conflict of interest.

Data Availability Statement

The data that support the findings of this study are available from the corresponding author upon reasonable request.

Keywords: DFT analyses · supercapacitors · polyaniline · polypyrrole: biopolymer composites

- [1] G. Wang, L. Zhang, J. Zhang, *Chem. Soc. Rev.* **2012**, *41*, 797.
- [2] M. Zhi, C. Xiang, J. Li, M. Li, N. Wu, *Nanoscale* **2013**, *5*, 72.
- [3] A. Viswanathan, A. N. Shetty, *Electrochimica Acta* **2018**, 289, 204.
- [4] B. Maria Mahimai, E. Li, J. Pang, J. Zhang, J. Zhang, *J. Energy Storage* **2024**, *96*, 112598.
- [5] A. Shokry, A. M. Elshaer, J. El Nady, S. Ebrahim, M. Khalil, *Electrochimica Acta* **2022**, *423*, 140614.
- [6] A. Thadathil, N. Edavan Chathoth, Y. A. Ismail, P. Anjukandi, P. Periyat, *J. Phys. Chem. C* **2022**, *126*, 16965.
- [7] D. Xiao, B. Sun, Y. Liu, E. Jiao, X. Wang, X. Chen, X. Cheng, K. Guo, K. Yuan, H. Zhang, *Polym. Polym. Compos.* **2025**, *33*, 09673911241304848.
- [8] Y. Xu, J. Wang, W. Sun, S. Wang, *J. Power Sources* **2006**, *159*, 370.
- [9] A. Laforgue, P. Simon, C. Sarrazin, J.-F. Fauvarque, *J. Power Sources* **1999**, *80*, 142.
- [10] S. Wustoni, D. Ohayon, A. Hermawan, A. Nuruddin, S. Inal, Y. S. Indartono, B. Yuliarto, *Polym. Rev.* **2024**, *64*, 192.
- [11] M. Kumar, S. K. Samal, T. Maharana, *Polym.-Plast. Technol. Mater.* **2025**, *64*, 309.
- [12] M. G. Tadesse, A. S. Ahmed, J. F. Lübben, *J. Compos. Sci.* **2024**, *8*, 53.
- [13] N. Ashok Kumar, J.-B. Baek, *Chem. Commun.* **2014**, *50*, 6298.
- [14] M. Lian, X. Wu, Q. Wang, W. Zhang, Y. Wang, *Ceram. Int.* **2017**, *43*, 9877.
- [15] R. Kandulna, R. B. Choudhary, R. Singh, *J. Inorg. Organomet. Polym. Mater.* **2019**, *29*, 730.
- [16] K. Wang, L. Li, Y. Liu, C. Zhang, T. Liu, *Adv. Mater. Interfaces* **2016**, *3*, 1600665.
- [17] Y. Kashyap, P. R., R. R. Pandey, A. Andola, D. H. Nagaraju, R. K. Pandey, *J. Solid State Electrochem.* **2024**, *28*, 3357.
- [18] Annu, S.-S. Park, M. N. Alam, M. Yewale, D. K. Shin, *Polymers* **2024**, *16*, 2907.
- [19] Y. Huang, H. Li, Z. Wang, M. Zhu, Z. Pei, Q. Xue, Y. Huang, C. Zhi, *Nano Energy* **2016**, *22*, 422.
- [20] D. Tian, H. Cheng, Q. Li, C. Song, D. Wu, X. Zhao, S. Hu, S. Chen, C. Hu, *Electrochimica Acta* **2021**, *398*, 139328.
- [21] Y. Xie, D. Wang, J. Ji, *Energy Technol.* **2016**, *4*, 714.
- [22] D. P. Dubal, S. V. Patil, G. S. Gund, C. D. Lokhande, *J. Alloys Compd.* **2013**, *552*, 240.
- [23] S. Chen, H. Cheng, D. Tian, Q. Li, M. Zhong, J. Chen, C. Hu, H. Ji, *ACS Appl. Energy Mater.* **2021**, *4*, 3701.
- [24] A. Viswanathan, A. N. Shetty, *Bull. Mater. Sci.* **2022**, *45*, 60.
- [25] K. Cheah, M. Forsyth, V.-T. Truong, *Synth. Met.* **1998**, *94*, 215.
- [26] M. A. Chougule, S. G. Pawar, P. R. Godse, R. N. Mulik, S. Shashwati, V. B. Patil, *Soft Nanosci. Lett.* **2011**, *2011*, 6.
- [27] S. Zuo, W. Liu, C. Yao, X. Li, Y. Kong, X. Liu, H. Mao, Y. Li, *Chem. Eng. J.* **2013**, *228*, 1092.
- [28] Y. Wang, J. Yang, L. Wang, K. Du, Q. Yin, Q. Yin, *ACS Appl. Mater. Interfaces* **2017**, *9*, 20124.
- [29] Z. Zhao, H. Wang, H. Huang, L. Li, X. Yu, *Colloids Surf. Physicochem. Eng. Asp.* **2021**, *626*, 127125.
- [30] P. Sharma, K. Singh, A. Kumar, D. Kumar, H. Mudila, U. Rednam, P. E. Lokh, R. e. Aepuru, A. Kumar, *ES Energy Environ.* **2024**, *24*, 1125.
- [31] S. T. Navale, A. T. Mane, A. A. Ghanwat, A. R. Mulik, V. B. Patil, *Measurement* **2014**, *50*, 363.
- [32] J. Stejskal, M. Trchová, P. Bober, Z. Morávková, D. Kopecký, M. Vrňata, J. Prokeš, M. Varga, E. Watzlová, *RSC Adv.* **2016**, *6*, 88382.
- [33] S. Goel, N. A. Mazumdar, A. Gupta, *Polym. Adv. Technol.* **2010**, *21*, 205.
- [34] C. Zhou, Y. Zhang, Y. Li, J. Liu, *Nano Lett.* **2013**, *13*, 2078.
- [35] Y. Shi, L. Pan, B. Liu, Y. Wang, Y. Cui, Z. Bao, G. Yu, *J. Mater. Chem. A* **2014**, *2*, 6086.
- [36] W. Wang, O. Sadak, J. Guan, S. Gunasekaran, *J. Energy Storage* **2020**, *30*, 101533.
- [37] J. Wang, J. Polleux, J. Lim, B. Dunn, *J. Phys. Chem. C* **2007**, *111*, 14925.
- [38] N. Elgrishi, K. J. Rountree, B. D. McCarthy, E. S. Rountree, T. T. Eisenhart, J. L. Dempsey, *J. Chem. Educ.* **2018**, *95*, 197.
- [39] S. Jain, S. Verma, S. P. Singh, S. N. Sharma, *Biosens. Bioelectron.* **2019**, *127*, 135.
- [40] G. P. Oliveira, B. H. Barboza, A. Batagin-Neto, *Comput. Theor. Chem.* **2022**, *1207*, 113526.
- [41] B. Seger, J. McCray, A. Mukherji, X. Zong, Z. Xing, L. Wang, *Angew. Chem.* **2013**, *125*, 6528.
- [42] P. Bätz, D. Schmeisser, W. Göpel, *Phys. Rev. B* **1991**, *43*, 9178.
- [43] S. Bouallag, A. Mougar, M. Zabat, A. Belayadi, *Phys. B Condens. Matter* **2024**, *695*, 416597.
- [44] M. Arjmandi, A. Arjmandi, M. Peyravi, A. K. Pirzaman, *Russ. J. Phys. Chem. A* **2020**, *94*, 2148.
- [45] N. Su, H. B. Li, S. J. Yuan, S. P. Yi, E. Q. Yin, *Express Polym. Lett.* **2012**, *6*, 697.
- [46] C. Ding, X. Qian, G. Yu, X. An, *Cellulose* **2010**, *17*, 1067.
- [47] L. D. Setiawan, H. Baumann, D. Gribbin, *Surf. Interface Anal.* **1985**, *7*, 188.
- [48] R. N. S. Sodhi, R. G. Cavell, *J. Electron Spectrosc. Relat. Phenom.* **1986**, *41*, 1.
- [49] E. J. Suoninen, T. D. Thomas, S. E. Anderson, M. T. Runyan, L. Ungier, *J. Electron Spectrosc. Relat. Phenom.* **1985**, *35*, 259.
- [50] A. Viswanathan, A. N. Shetty, *J. Phys. Chem. Solids* **2024**, *193*, 112141.
- [51] P. Saharan, M. Singh, C. Kumar, S. Sundriyal, S. R. Dhakate, *ACS Appl. Nano Mater.* **2023**, *6*, 21909.
- [52] X.-Y. Tao, Y. Wang, W. Ma, S.-F. Ye, K.-H. Zhu, L.-T. Guo, H.-L. Fan, Z.-S. Liu, Y.-B. Zhu, X.-Y. Wei, *J. Mater. Sci.* **2021**, *56*, 16028.
- [53] Y. Wang, W.-B. Ma, L. Guo, X.-Z. Song, X.-Y. Tao, L.-T. Guo, H.-L. Fan, Z.-S. Liu, Y.-B. Zhu, X.-Y. Wei, *J. Mater. Sci. Mater. Electron.* **2020**, *31*, 6263.

Manuscript received: May 1, 2025

Revised manuscript received: June 12, 2025

Version of record online: